Improved corrosion resistance of aluminum brazing sheet by a post-brazing heat treatment

Norouzi Afshar, F.; Tichelaar, F. D.; Glenn, A. M.; Taheri, P.; Sababi, M.; Terryn, H.; Mol, J. M.C.

DOI
10.5006/2210

Publication date
2017

Document Version
Accepted author manuscript

Published in
Corrosion: journal of science and engineering

Citation (APA)
Norouzi Afshar, F., Tichelaar, F. D., Glenn, A. M., Taheri, P., Sababi, M., Terryn, H., & Mol, J. M. C. (2017). Improved corrosion resistance of aluminum brazing sheet by a post-brazing heat treatment. *Corrosion: journal of science and engineering*, *73*(4), 379-393. https://doi.org/10.5006/2210

Improved corrosion resistance of aluminum brazing sheet by a post-brazing heat treatment

F.N. Afshar*,**, F.D. Tichelaar***, A.M. Glenn****, P. Taheri**, M. Sababi**, H. Terryn**,*****, J.M.C. Mol‡,**

Keywords: aluminum alloy, microstructure, heat treatment, Kelvin probe, Transmission electron microscopy

‡ Corresponding author: +31152786778
Email: (e-mail: J.M.C.Mol@tudelft.nl).

* Materials innovation institute (M2i), Elektronicaweg 25, 2628 XG Delft, The Netherlands

** Delft University of Technology, Department of Materials Science and Engineering, Mekelweg 2, 2628 CD Delft, the Netherlands

*** Delft University of Technology, Kavli Institute of Nanoscience, National Centre for High Resolution Electron Microscopy, Lorentzweg 1, 2628 CJ Delft, The Netherlands

**** CSIRO Mineral Resources, Clayton, Victoria, Australia

***** Vrije Universiteit Brussel, Research group Electrochemical and Surface Engineering, Pleinlaan 2, B-1050 Brussels, Belgium

Abstract

This work studies the influence of the microstructure on the corrosion mechanism and susceptibility of as-brazed aluminum sheet. Various microstructures are obtained using post-brazing heat treatments developed to enhance the corrosion resistance of an AA4xxx/AA3xxx brazing sheet. The heat treatment results in a decrease of the matrix Si content within the heat affected zone (HAZ) and an increase of the Si fraction in the α-Al(Fe-Mn)Si phase. Additionally, the effect of the heat treatment on the local electrochemical activity and corrosion properties are studied. The results indicate that the corrosion susceptibility of the as-brazed structure is diminished due to an amendment of the local electrochemical behavior of the outer clad surface after the post-brazing heat treatment. Moreover, the potential difference between the clad material and core is increased resulting in an improved sacrificial cathodic protection of the core by the re-solidified clad layer.

INTRODUCTION

In the modern automotive industry, cost reduction is a necessity and the expensive long life (LL) as-brazed alloys become less competitive. There is a high demand for low cost alloys, while excellent corrosion resistance comparable to that of the expensive LL alloys is required as well [1-5]. Standard AA3003 and AA3005 alloys exhibit poor corrosion resistance [3], however, they are more cost effective as compared to the LL alloys [3]. Therefore, improving the corrosion resistance of as-brazed aluminum sheet is of both scientific and industrial interest. The pivotal role of intermetallic particles in electrochemical properties and corrosion performance of the aluminum alloys have been studied and correlated to formation of microgalvanic cells [6-12]. Moreover, the effects of the corrosive media on the corrosion performance of the as-brazed aluminum radiators has been studied. It was inferred that the standard laboratory seawater acetic acid test (SWAAT) hardly mimics the real life performance in different conditions [13]. Iwao et al. [14] showed that the chloride ions of hydrochloric acid accelerate pitting corrosion, whereas acetic acid prompts general dissolution of the AA3003 as-brazed aluminum alloy.

The influence of heat treatment on the corrosion susceptibility of aluminum alloys has been evaluated as well [6, 15-26]. We studied the effect of heat treatment on filiform corrosion (FFC) susceptibility of the rolled aluminum alloy AA3005 at the 150–500°C heat treatment range[6]. We found that the corrosion resistance is reduced significantly by an elevated annealing temperature, i.e. > 350°C, while the high temperature promotes formation of fine intermetallic particles and noble alloying elements in the superficial surface layer leading to a significant loss of the FFC resistance. We also investigated the combined effects of heat treatment and cleaning process on filiform corrosion resistance of AA3005 and AA5754 alloys. [15] We reported that the high-temperature heat treatment significantly degrades the filiform corrosion resistance of alloy AA3005, whereas application of a commercial acid cleaning and a chromating pre-treatment resulted in negligible improvements of the FFC resistance. Even, a moderate reduction of the FFC resistance was observed for AA5754 alloy attributed to the poor protective properties of a thick- and magnesium enriched-oxide layer formed during the annealing process. Andreatta et al. reported that the corrosion behavior of AA7075 is influenced by the microstructural variations driven by heat treatment [16]. Zhang et al. [26] investigated the effects of both solution heat treatment and artificial ageing on the metallurgical processes taking place. These processes include dissolution and coarsening of particles, precipitation, distribution and density variation of the dislocations, and compositional and structural changes of the grains and grain boundaries, which in turn influence the mechanical and corrosion properties of the treated aluminum alloys.

Sánchez-Amaya et al. [23] investigated the intergranular corrosion (IGC) susceptibility of aluminum alloys subjected to the heat treatments using metallographic analyses and electrochemical noise measurements. A correlation between the IGC susceptibility and noise data was hardly detected because of the high electrochemical activity of the investigated substrate and the low signal-to-noise ratio of the data collected. Marlaud et al. [22] investigated the exfoliation corrosion (EFC) mechanism of 7XXX aluminum alloys versus heat treatments. It was found that the current and potential transients play important roles in the EFC mechanism, while propagation of intergranular cracks are influenced dramatically by the transients. They also reported that the number of transients and consequently EFC susceptibility in-turn is decreased by over-aging heat treatments. Chen et al. [17] explained the influence of heat treatment on EFC of AA7085 aluminum alloy due to precipitates formed within the matrix grain boundaries during a re-aging process. The results showed that re-aging improves the EFC resistance without degrading the mechanical properties. El-Menshawy et al.[18] found that the corrosion mechanism is governed by the aging regime influencing the precipitate type, size and distribution.

Finnegan and Woods [19] developed a post-brazing heat treatment to improve the corrosion resistance of vacuum brazed heat exchangers. The mechanism behind the improved corrosion resistance was correlated to the precipitation of dispersoid phases during the heat treatment. The treatment was claimed to eliminate sensitivity to the

classic IGC of the as-brazed aluminum components due to profusion of local micro-galvanic cells overruling the conventional grain boundary solute enrichment process and the adjacent relatively precipitate-free grains [27-29]. Other studies on AlMgSiCu alloys evaluate the effects of heat treatments on micro-galvanic coupling between grain boundary precipitates and the depleted zones [24, 25, 30]. It was concluded that the IGC resistance is achieved by lowering the Cu content or conducting an appropriate heat treatment if high Cu content is inevitable. They concluded that formation of discontinued Cu films at grain boundaries and depletion of hardening phases are the major phenomena improving the IGC resistance of AlMgSi(Cu) model alloys [31].

Iwao and Asano [20] utilized sea water acidified accelerated test (SWAAT) [4] to evaluate the corrosion behaviour of post-brazing heat treated aluminum sheets. It was shown that the corrosion depth of Al-1%Mn and Al-1%Mn-0.5%Si alloys is reduced by the heat treatment, while that of Al-1%Mn-0.5%Si-0.5%Cu alloy is increased accompanied by considerable IGC attack. The authors also investigated the effect of Cu and Mg on IGC susceptibility of AA3xxx alloys subjected to SWAAT after brazing at 600°C followed by a post-brazing heat treatment at 200°C for durations of 1 to 10 hours [21]. IGC was observed for the alloy with Cu additives correlated to a selective dissolution of the Cu depleted zones. Moreover, pitting corrosion was observed for the alloy containing Cu and Mg elements, while Cu-rich precipitates were observed in the grains and grain boundaries. The authors concluded that a diminished IGC susceptibility is expected from a smaller potential difference between the depleted zone and grain matrix. Additionally, the Mg element present in Al-Mn-Si-Cu alloy improves the corrosion resistance after applying a post-heat treatment [21].

Figure 1 summarizes the previous microstructural characterizations of the materials under investigation [2, 32]. Figure 1a shows cross-sectional micrographs of a precipitate-free heat affected zone (HAZ). HAZ is formed due to a progressive interaction between the liquid and core interfaces altering the alloying element distribution [33, 34]. Among the alloying elements, Si may diffuse up to 40 μm [2, 32]. Figure 1b exhibits an optical image of the surface microstructure subjected to brazing and consequently accumulation of the α-Al(Fe-Mn)Si phase. Figures 1c shows cross-section images and Si and Cu distribution profiles before and after the brazing process [2, 35-37]. It is shown that the Si content increases after the brazing (~1 wt% [37]), while a gradual decrease with depth is noticeable. However, the Cu concentration profile depicts a minimum Cu content (~0.25 wt% [35]) in the middle of the pre-eutectic aluminum grains and a maximum Cu content (~0.6 wt% [35]) in the Al-Si eutectic at the surface and within the grain boundaries. Full electrochemical characterizations have been conducted at macro- [2], localized- [35] and micro- scales [36, 37] and correlated to the microstructure as a consequence of the brazing treatments. The investigations revealed that the brazing processes lead to localized corrosion susceptibility of the core and clad materials and decrease the sacrificial cathodic protection capability of the re-solidified clad structure towards the core material [2, 4, 32, 35-37]. A correlation between the microstructure and electrochemical reactivity implies that applying the post-brazing heat treatment may enhance the corrosion resistance of the aluminum as-brazed sheet [37].

FIGURE 1

This work aims to propose a post-brazing heat treatment and investigate the effects of the treatment on the corrosion resistance of the as-brazed aluminum sheet. We utilize thermodynamic calculations as well as microstructural and electrochemical characterization techniques to define ranges of the heat treatment temperature and time. We also evaluate the corrosion mechanism of the structures as a result of the heat treatment process applied.

EXPERIMENTAL PROCEDURES

Materials

AA3xxx aluminum sheets were cut to 210 × 297 mm and cladded with AA4xxx on one side. X-Ray Fluorescence (XRF) analyses were conducted on the clad material and core using PW2400 equipment and UniQuant software as summarized in Table 1.

Table 1

Brazing procedure

The brazing process was done in dry condition using nitrogen gas in a Controlled Atmosphere Brazing (CAB) furnace at 600 ˚C for 3 min followed by ramping down to room temperature at 60 ˚C/min. The brazing temperature was around the clad material liquid temperature (612 ˚C) [38] and below the core material solidus temperature (640 ˚C) [2].

Thermodynamic calculations

The thermodynamic calculations were conducted using JmatPro (Version 6.0) software. This version enables calculation of the physical properties for thermodynamic purposes [39], based on minimization of the free energy at a defined composition and temperature. The minimum free energy is the state that the system equilibrium [2]. Therefore, the software predicts the material characteristics including the stable and metastable phase equilibria in certain conditions. The software also predicts the chemical composition changes of a certain phase over a range of temperatures.

X-ray micro analysis (XMA)

A Bruker field emission SEM integrated with an energy dispersive spectrometer (EDS) and X-ray micro analysis (XMA) mapping was used to analyze the chemical composition of the cross sections. A 15 nm - thick carbon layer was applied on the surfaces to provide the required conductivity for the measurements. The electron beam energy and the probe current were 15 kV and 10 nA, respectively to provide a resolution of 800 × 690 pixels for the mapping.

FE-EPMA analysis

The field emission electron microprobe was a JEOL 8500F model with an EDS and a top-referenced sample holder was used for the electron probe micro analysis (EPMA) mapping. The x-rays signals of Mn Lα, Fe Lα, Cr Lα, Si Kα and Cu Lα were collected by tuning a wavelength dispersive spectrometer (WDS), while EDS was utilized to analyze the other elements. The EPMA maps were processed by means of Chimage software [40].

TEM analysis

Transmission electron microscope (TEM) examination was conducted in a Tecnai-F20ST TEM/STEM operated at 200KV. The samples were prepared by gluing glass on both sides of the as-brazed sheets. Subsequently, the sheet materials were cut to make cross-sections of 0.5 mm thick which were polished down to 20 μm. The thinning was continued using a Gatan PIPS 691 ion mill operated with an Ar beam to obtain electron transparency. High angle annular dark field (HAADF) and Bright field (BF) images were collected. To make a diffraction contrast for the BF mode, the undiffracted beam option was chosen. For the HAADF images, high angle scattered electrons were detected on a ring shape detector. Hence, the brightness of each pixel represents the amount of high angle scattered electrons. For a certain TEM foil thickness, a high brightness means an element with high atomic number. Elemental compositions were studied with an X-ray

energy dispersive spectrometry (EDS) using a local electron probe and an EDAX system integrated with the Tecnai operating software.

Atomic force microscopy (AFM) and scanning Kelvin probe force microscopy (SKPFM) analyses

Volta potential measurements of the samples were collected using an AFM/SKPFM tool equipped with a digital instrument Nanoscope III multimode as described in details elsewhere [33]. The measurements were conducted in ambient air. Potential differences and topographical maps were measured using a pixel density of 256 x 256. The tips were made of antimony (n) doped silicon coated with 20 nm platinum/iridium on both sides with 0.01-0.025 Ω.cm resistivity. The cantilever was 200-250 µm long, 23-33 µm wide and 2.5-3.5 µm thick. The samples were polished using the finest grade of 0.25 µm and ion-polished on the cross sections intended to make smooth surfaces by polishing away a superficial layer of the clad material. < 5kV was used for the Ar ion beam to etch the cross sections. Cross-sections of the as-brazed and post-brazing heat treated samples were made by a cross-section ion polisher, model JEOL, SM-09010 followed by an ultrasonic cleaning step in ethanol. Throughout the manuscript, the Volta potential differences between the surface and tip is named "VPD", whereas, the Volta potential difference between the various sample features is called "VPD difference". Note that the VPD measurements are conducted versus AFM tips, [36] the Volta potentials of which vary across the differently coated tips with dissimilar oxide layers [41, 42]. This necessitates calibration of the VPD values with a reference material.

Electrochemical analysis

A Solartron potentiostat was used for the potentiodynamic polarization (PD) measurements consisting of working, reference and counter electrodes. A rounded sample with a diameter of 20 mm formed the working electrode while the reference counter electrodes were a saturated calomel electrode (SCE) and a platinum (Pt) grid, respectively, placed in a homemade electrochemical cell. The SWAAT solution [4] contained 42 g/l of NaCl and 10 ml/l of CH_3COOH (glacial acetic acid) adjusted with 10 wt% NaOH to obtain a pH value of about 3.0. The electrochemical measurements were conducted in ambient with no stirring or deaeration. The anodic branch of the PD measurements were carried out between 10 mV below and 1 V above the OCP, while the cathodic branch was within 10 mV above and 450 mV below the OCP. Each PD experiment was started after 15 min OCP measurement with 0.5 mV/s scan rate. Each measurement reported in this study was repeated for three times to check the result reproducibility.

Corrosion mechanism investigation

SWAAT is a well-known technique to evaluate the morphology of heat exchanger substrates, e.g. as-brazed aluminum sheet, after corrosion reflected in PD performances [4]. Moreover, analysis of the clad side after the anodic polarization step provides further insight of the corrosion mechanism. In this study, the corrosion resistance investigation was done by a direct exposure of the both as-brazed and post-brazing heat treated samples to SWAAT solution in a simulated SWAAT cabinet for different periods followed by optical micrograph analyses of the cross-sections.

Results

Determination of the optimal temperature and time for the post-brazing heat treatment

In order to foresee the equilibrium phases and the compositional changes taking place at the 25-600 °C temperature range, thermodynamic calculations were conducted. The results are presented in Figures 2 and 3. Figure 2 shows that Si, α-Al(Mn-Fe)Si and Al_2Cu are the equilibrium phases existing in the re-solidified clad structure. At temperatures between 330 °C and 570 °C, a complete dissolution of the Al_2Cu particles takes place, while above 570 °C, an increase of the Si solubility in the aluminum matrix is observed. However, the highest phase fraction of α-Al(Mn-Fe)Si particles is achieved at about 330 °C. Figure 3 shows composition changes of α-Al(Mn-Fe)Si particles within the 100-600 °C temperature range. The maximum Si and Cu contents in the α-Al(Mn-Fe)Si phase exist at 218 °C and 336 °C, respectively. Furthermore, it can be seen that a high temperature (>500 °C) increases the Fe and decreases the Mn contents of the α-Al(Mn-Fe)Si particles. Therefore, the temperature range of 330-570 °C is considered to enhance the corrosion resistance, while 336 °C is selected for further analysis providing optimal corrosion resistance for the modified as-brazed aluminum sheet studied.

FIGURE 2

FIGURE 3

SKPFM analysis is used to estimate the optimal heat treatment time. Figures 4 and 5 show the VPD values and line scan section analyses of surfaces subjected to post-brazing heat treatments. In the VPD maps, Si particles, i.e. with a brighter contrast, are considered as local references for the VPD difference maps of the as-brazed and post-brazing heat treated samples as discussed elsewhere [36]. VPD differences of the Si and matrices is compared using the section analyses before and after the post-brazing heat treatments for 5, 10, and 20 hours at 336 °C. Figure 4 shows the positions of the sectioning profiles. Three line profiles were investigated for each sample as shown in Figure 5. The peak potential is corresponding to the VPD of Si which is about 300 mV. A comparison of the graphs indicates that the brazing process increases the matrix VPD, while the post-brazing heat treatment counteracts this effect. Brazing processes at 336 °C for 5, 10 and 20 hours increase the VPD difference of the Si and matrix by 20, 50 and 60 mV, respectively, versus the 300 mV VPD difference of the Si and matrix.

FIGURE 4

FIGURE 5

Characterization of the post-brazing heat treated samples

Microstructural characterization

X-ray micro analysis

Figure 6 shows the maps of X-ray micro analysis for Si and Cu as well as the images of SEM backscattered electron of the as-brazed and post-brazing heat treated samples at 336 °C for 20 hours. The core material and re-solidified clad region are distinguished clearly. Regions 1 and 2 representing the Al-Si eutectic phase are marked in the Si map of the as-brazed sample. The Cu contents are obviously different among these two eutectic regions while the Al-Si eutectic (2) is Cu-enriched and the Al-Si eutectic (1) is Cu-lean as indicated by the Cu map. Grain boundaries of the re-solidified clad are marked with white dashed lines in the Cu map. The eutectic Al-Si phases are formed during the last stage of solidification and between the grains of pre-eutectic Al

crossing the grain boundaries. The most important effects of the brazing in the Cu map of the as-brazed sample are the non-homogeneous dispersion of Cu within the re-solidified clad substrate and accumulation of Cu-rich intermetallics, e.g. Al_2Cu, α-Al(Fe-Mn)Si) at grain boundaries. The Si map of the post-brazing heat treated sample shows a greater density of Si particles in the HAZ and diffusion zone as compared to that of the as-brazed material. The Cu map of the post-brazing heat treated samples shows a uniform dispersion of the Cu element within the re-solidified clad substrate. No clear difference between the Cu concentrations of the Al-Si eutectic regions, with and without IMPs, is detected.

FIGURE 6

EPMA analysis

Figures 7 and 8 show the Cu and Si FE-EPMA maps of the as-brazed and post-brazing heat treated samples at 336 °C for 20 hours. The Cu concentration maps indicate that the brazing treatment results in formation of Cu-lean and Cu-accumulated areas in the Al-Si eutectic region of the re-solidified clad substrate and within eutectic grain boundaries (GBs) of the Al matrix. Moreover, the brazing treatment leads to precipitation of Cu-rich intermetallics. On the other hand, the Cu concentration map of the post-brazing heat treated sample reveals no Cu accumulation within the Al-Si eutectic regions, although a non-uniform Cu dispersion is visible in the re-solidified clad substrate. A comparison of the Si FE-EPMA maps of the as-brazed and post-brazing heat treated samples in Figure 8 confirms heavy precipitation of Si particles in the HAZ and diffusion zone (DZ) as a result of the post-brazing treatment.

FIGURE 7

FIGURE 8

TEM analysis

Figures 9-11 shows the TEM results. Figures 9a and c exhibit typical TEM micrographs of the core and clad regions of the as-brazed and post-brazing heat treated samples. A mosaic structure is formed in both clad material and core of the as-brazed sample due to the presence of dislocation walls forming sub grains of typically 300 nm diameter. Si particles and α-Al(Fe-Mn)Si phase can also be detected near high-angle grain boundaries (GB) of the as-brazed clad material, as shown in Figure 9a (GBs are not visible in the image). The mosaic structure of the as-brazed core material makes distinction of the intermetallic particles difficult. The post-brazing heat treated samples also lacks the mosaic structure due to the annealing process as shown in Figures 9a and c.

Figure 10 depicts the presence of dislocations in the post-brazing heat treated samples. The clad material of the post-brazing heat treated samples show larger Si and Si containing (α-Al(Mn,Fe)Si) particles compared to the as-brazed clad material. The GBs of the clad and core structures of the post-brazing heat treated samples are presented in Figures 10 and 11, respectively. A high angle GB between the two grains is shown in Figure 10. The orientation difference between the grains leads to a strong contrast in the micrograph. Two-line scan elemental analyses have been carried out across the GB in Figure 10. Figure 11 summarizes the GB investigation of the core structure of a post-brazing heat treated sample. Figure 11a confirms the presence of the Si and Figure 11c verifies formation of α-Al(Fe-Mn)Si phase at the grain boundaries upon the post-brazing heat treatment. Figure 11d shows several line scan analyses verifying no Cu segregation at the GBs of the post-brazing heat treated core material.

FIGURE 9

FIGURE 10

FIGURE 11

Electrochemical characterization

OCP and PD measurements

Figure 12 presents the OCP profiles of the post-brazing heat treated the clad material and the core after 900s stabilization. A 15 mV potential difference between the clad material and core is detected. Figure 13 shows the cathodic and anodic behavior of the as-brazed and post-brazing heat treated clad materials. As shown in Figure 13a, similar anodic behaviors are detected for the as-brazed and post - brazing heat treated clad materials, while the current density fluctuates around the OCP. However, the heat treated clad material shows a higher reactivity in the cathodic branch as compared to that of the as-brazed material.

FIGURE 12

FIGURE 13

AFM and SKPFM analyses

Figure 14 shows the VPD and topographical images as well as the line scan analyses of the as-brazed and post-brazing heat treated samples. Bright Si particles/needles are exhibited clearly in the VPD maps. The surface roughness is in the nm range as shown in Figures 14c and 14d indicating reliable Volta potential measurements [36]. A comparison of the Si particle and the matrix VPDs of the as-brazed and post-brazing heat treated materials has been performed using the section analysis method as shown in Figures 14a and b. Three profile lines are collected per sample, while the VPD of Si is utilized as the reference [36]. Figure 15 presents the VPD values and statistical parameters of the as-brazed and post-brazing heat treated samples reported in separate boxes. The boxes are defined by the 25th and 75th percentiles, whereas the whiskers are determined by the 5th and 95th percentiles. Moreover, the values of minimum, maximum, mean and median are included in the figure. The matrix VPDs of the heat treated clad material are lower than those of the as-brazed clad material. Additionally, the VPD average values of the matrices subjected to the post-brazing heat treatment drop by 50 mV vs the Si needle references.

Figure 16 shows the topographical and VPD maps of cross sections of the as-brazed and post-brazing heat treated samples in the HAZ. Figures 16a and b indicate the presence of some contamination (bright dots) even after an ultrasonic cleaning step. Figures 16c and d show that the post-brazing heat treated material possesses a higher density of nobler particles than that of the as-brazed sample.

FIGURE 14

FIGURE 15

FIGURE 16

Corrosion morphology

Figure 17 shows the cross sectional micrographs of the as-brazed and post-brazing heat treated materials subjected to anodic polarization at 1V vs OCP values. Figures 17a, b and c shows that the clad material provides a limited corrosion protection for the core material of the as-

brazed samples. Clear dissolved clad material and core subjected to corrosion at the pre-eutectic aluminum grains as well as localized corrosion of the clad and core materials, i.e. IGC and pitting, are visible in the images. Figures 17d, e and f depict that the post-brazing heat treated material shows a relatively uniform and less severe corrosion.

FIGURE 17

Figure 18 shows the cross sectional micrographs of the as-brazed and post-brazing heat treated samples after 30 days exposed to the simulated SWAAT. It is exhibited that the heat treatments enhance the corrosion resistance. After 30 days of the SWAAT exposure, disintegration of the as-brazed material is observed, while the re-solidified clad substrate of the heat treated one is subjected to a uniform dissolution.

FIGURE 18

Discussion

An appropriate post-brazing temperature range is determined to eliminate the microstructural features that result in poor corrosion resistance. The harmful microstructural changes due to the brazing process include an increase of the matrix Si and Cu content in the HAZ, Cu non-uniform dispersion in the HAZ, precipitation of intermetallic particles (Al_2Cu, α-Al(Fe-Mn)Si and Si) in the grain boundaries, accumulation of Cu at the surface and in Al-Si eutectics and formation of intermetallics in Al-Si eutectic phases [2, 32, 35-37]. These microstructural features were found to rise the VPD of the re-solidified clad substrate leading to localized corrosion of the brazed core and clad structures and reduced capability of the sacrificial cathodic protection [36, 37].

The thermodynamic calculations (Figure 2) indicate that annealing temperatures below 570 °C increase the equilibrium amount of Si particles in the structure. Therefore, such a treatment is expected to reduce the Si amount of the re-solidified clad substrate due to the saturated state of Si in solid solution [37]. This in turn reduces corrosion potentials of the re-solidified clad substrate and diffusion zone making the outer layers of the post-brazing heat treated structure more anodic than the core material.

Moreover, the corrosion resistance of as-brazed structures can be upgraded by eliminating the Al_2Cu intermetallic particles, exhibiting a high cathodic reactivity, precipitating at grain boundaries [37]. Heat treatments above 330 °C dissolves the Al_2Cu particles expected to improve the localized corrosion susceptibility (IGC and pitting) of the core and the clad materials. Additionally, a heat treatment between 330 °C and 570 °C increases the amount of α-Al(Fe-Mn)Si precipitates in the HAZ and diffusion zone leading to a reduction of the noble alloying elements (Si and Mn). This further decreases the corrosion potentials of the HAZ and diffusion zone making them more anodic and consequently protective towards the core material. Another advantage of this type of cathodic precipitations distributed in the HAZ and diffusion zone are profusion of local micro-galvanic cells dominating the observed grain boundary segregation phenomena upon a brazing treatment [19]. This eliminates the localized corrosion susceptibility (pitting and IGC) of the brazed structure. The effect is extended across the thickness of the post-brazing heat treated material in the HAZ and the diffusion zone. The treatment also results in a more uniform dispersion of the Cu element in the re-solidified clad substrate.

Thermodynamic calculations (Figure 3) show that the chemical composition of the α-Al(Fe-Mn)Si phase is also temperature dependent. Although heat treatment at 218 °C is expected to further decrease the Si amount of the matrix (by increasing the Si content of the alpha particles), Al_2Cu particles are insoluble below 330 °C. On the other hand, the heat treatment temperature of 336 °C increases the Cu content of the α-Al(Fe-Mn)Si phase to its maximum level, while the α-Al(Fe-Mn)Si phase accommodates a portion of the Cu content precipitated at the topmost surface of the as-brazed structure [2, 32, 35]. Therefore, a heat treatment at 336 °C improves the corrosion resistance by enhancing the sacrificial behavior of the topmost layer to cathodically protect the core structure.

Heat treatments at 336 °C for 5, 10 and 20 hrs, increase the VPD difference of Si and the clad matrix presumably due to a reduction of the Si in α-Al(Fe-Mn)Si phase due to the Si precipitation. This decreases the nobility of the clad matrix versus the core material improving the sacrificial properties of the clad matrix for protection of the core material [36]. The 60 mV potential reduction achieved after 20 hrs of post-brazing heat treatment (Figure 5) is expected to provide the maximum possible sacrificial protection offered by the re-solidified clad substrate. This corresponds to the same protection condition before the brazing treatment. Therefore, 20 hrs of heat treatment was selected as an appropriate duration for the material investigated. Note that a shorter treatment time, e.g. 10 hrs, may also provide some protection properties, however, variations of the microstructural features and electrochemical behaviors are expected to be more pronounced at the longer treatment times, i.e. 20 hrs.

A comparison of the Si and Cu X-ray micro-analysis mapping before and after the post-brazing heat treatment reveals the beneficial influences of the proposed post-brazing heat treatment. The improvements include a more uniform distribution of the Cu amount in the re-solidified clad substrate, elimination of the Cu-rich eutectics/GBs and a higher density of Si-containing particles formed. These are expected to provide a better corrosion protection for the core material and eliminate the localized corrosion susceptibility of the brazed structure.

The FE-EPMA analysis of the Cu and Si contents and distributions further confirm the beneficial effects of the post-brazing heat treatment. A Cu map comparison of the as-brazed and post-brazing heat treated samples clearly show elimination of the Cu at the surface. The difference of the Cu concentration in the Al-Si eutectic phases and the pre-eutectic aluminum grains is reduced as well exhibiting the role of the heat treatment in homogenizing the re-solidified clad substrate composition. Moreover, the FE-EPMA Si maps of the as-brazed and post-brazing heat treated samples clearly demonstrate the increase of Si and Si containing particles (α-Al(Fe-Mn)Si phase) in the HAZ and diffusion zone. Therefore, a reduced OCP value of the re-solidified clad substrate is expected due to the nobble nature of Si [3].

The decrease of dislocation density and the absence of the mosaic structure in the post-brazing heat treated material (core and clad) are expected to provide a thermodynamically stable material leading to a better corrosion resistance. This is another advantage of the proposed heat treatment process which could hardly be revealed using the previous characterization techniques. The presence of a higher particle concentration in the structure of the post-brazing heat treated clad material (Figure 9b) verifies the assumptions.

No Cu segregation at the GBs of the clad material and the core after the post-brazing heat treatment is expected which is presumably the main reason of the observed elimination of the localized corrosion susceptibility. However, the presence of Si particles in GBs of the post-brazing heat treated samples leads to IGC due to the selective dissolution of the material adjacent to grain boundaries containing a

lower concentration of Si. In contrast, no IGC attack was observed likely due to the fact that the treatment eliminates formation of Si depleted zones by stimulating further Si and α-Al(Fe-Mn)Si precipitation at and adjacent to the grain boundaries. This further supports the idea that an increased amount of the local micro-galvanic cells leads to a higher amount of the cathodic sites dominating GB segregation precipitation at the adjacent free zone.

The OCP results (Figure 12) show a negligible potential change between the clad and core materials due to the post-brazing heat treatment. OCP values of the as-brazed clad material are reported elsewhere [36]. The OCP profile of the post-brazing heat treated clad material stabilizes around -720 mV while that of the as-brazed clad material is reported to be around -710 mV [36]. Therefore, the post-brazing heat treatment leads to a 10 mV potential drop of the clad material.

The anodic polarization curves (Figure 13a) indicate IGC or pitting corrosion of the material studied. The potentials above -600 mV depict an increase of the current density between 10^{-3} and 10^{-1} Acm^{-2}. Similar anodic polarization responses of the as-brazed and post-brazing heat treated clad materials indicate comparable corrosion rates in the SWAAT environment, although the attack mechanism could be different [2]. The sudden increase of the current density around the OCP implies susceptibility of the studied surfaces to localized corrosion. The higher cathodic reactivity of the post-brazing heat treated clad material is correlated to a reduced density of the cathodic precipitates (Si and α-Al(Fe-Mn)Si).

To obtain a detailed interpretation of the localized corrosion behavior, AFM/SKPFM measurements are carried out. The results show that the silicon needles of the as-brazed and post-brazing heat treated alloys exhibit higher VPD values than that of the aluminum matrix. It has been reported that Si dissolves only up to 0.015 wt % of aluminum [36] indicating stability of the Si phases subjected to the brazing treatments. Therefore, Si is a reliable local reference for the Volta potential measurements of as-brazed aluminum sheets [36,37].

In this study, Si particles are selected as the local references subjected to minimal Volta potential variations due to the heat treatments. VPDs indicate an average decrease of 50 mV for the matrixes due to the heat treatment at 336 °C for 20 hrs (Figure 15). This VPD decrease is due to precipitation of the Si and α-Al(Fe-Mn)Si phase in the clad material as indicated by the 10 mV OCP drop as well [36]. Therefore, the sacrificial cathodic protection of the core by the re-solidified clad substrate is improved leading to a diminished pitting susceptibility of the deeper layers [35].

Note that the reduced VPD of the clad material can be correlated to an increase of the VPD difference between Si and the clad material increasing the galvanic interaction between the clad material and cathodic sites and promoting localized corrosion [36]. Other investigations [2, 35-37] together with the morphological studies of this work indicate that the latter interpretation is not valid for all cases. Accordingly, Si is not an effective cathodic material versus the aluminum matrix due to a negligible oxygen reduction even though Si possesses a nobler corrosion potential with respect to aluminum [2, 3, 35-37, 43]. A comparison of the cross-sectional VPD maps in the HAZ of the as-brazed and post-brazing heat treated materials shows that the post-brazing heat treatment leads to precipitation of nobler particles versus the aluminum matrix. This further confirms the FE-EPMA and TEM microstructural characterization results. However, a micro-level electrochemical investigation is required to obtain a detailed understanding of the reactivate microstructural features.

Pitting and intergranular corrosion (IGC) are the observed degradation mechanisms of the as-brazed material, while the post-brazing heat treated clad material presents a relatively uniform corrosion mechanism. Figure 17 shows that the as-brazed material is subjected to extensive IGC, however, the post-brazing treatment prevents heavy localized corrosion and limits the corroded area only to the re-solidified clad layer. Additionally, cross-sections of the as-brazed and post-brazing heat treated materials after the SWAAT exposure imply the importance of the post-brazing heat treatment to develop the sacrificial properties of the re-solidified clad substrate to cathodically protect the core material. It is worth mentioning that susceptibility of the core material to localized corrosion is eliminated as well. This is attributed to the precipitation and uniform distribution of intermetallic particles (Si and α-Al(Fe-Mn)Si) and re-distribution of the alloying elements (Cu and Si) [37].

This study shows the beneficial effect of the post-brazing heat treatment on the local corrosion resistivity of the as-brazed aluminum sheets. Further research is required to evaluate the effects of the residue materials, e.g. those formed due to the Mg segregating to Si, on the electrochemical and corrosion performances of the post-brazing aluminum substrates.

CONCLUSIONS

This work presents the effect of a post-brazing heat treatment to enhance the corrosion resistance of a modified AA4xxx/AA3xxx as-brazed sheet based on thermodynamic calculations and experiments.

- It is shown that the corrosion resistance of an as-brazed aluminum sheet can be improved substantially by application of a post-brazing heat treatment.
- Using thermodynamic calculations and SKPFM analyses, the post-brazing heat treatment parameters, i.e. temperature and time can be optimized.
- An enhanced corrosion resistance is obtained due to formation of an efficient sacrificially protecting layer and elimination of the intergranular and pitting corrosion sensitivity of the as-brazed clad and core structures.
- The post-brazing heat treatment decreases the VPD of the re-solidified clad material in turn increasing the sacrificial cathodic protection capability of the material. The VPD drop due to the heat treatment is approximately 50 mV accompanied by an OCP drop.
- The post-brazing heat treatment uniformly distributes the Cu amount in the re-solidified clad structure dissolving Al_2Cu precipitates at the grain boundaries and increases the concentration of Si and α-Al(Fe-Mn)Si phase in the HAZ and the diffusion zone.
- Local electrochemical activity and corrosion performance tests indicate diminished localized corrosion susceptibility and enhanced sacrificial cathodic protection of the core material by the re-solidified clad of the post-brazing heat treated samples.

ACKNOWLEDGMENTS

This work was conducted under the project number M21.6.08317 in the framework of the research program of Materials innovation institute M2i (http://www.m2i.nl).

REFERENCES

1. S. Iwao, M. Yoshino, M. Edo, S. Kuroda, Corrosion 71, 5 (2015): p. 598-605.
2. F.N. Afshar, J.H.W. de Wit, H. Terryn, J.M.C. Mol, Corrosion Science 58, (2012): p. 242-250.
3. S.D. Meijers, "Corrosion of Aluminium Brazing Sheet" Diss Delft 2002, Corus Technology,
4. F.N. Afshar, E. Szala, A. Wittebrood, R. Mulder, J.M.C. Mol, H. Terryn, J.H.W. de Wit, Corrosion Science 53, 12 (2011): p. 3923-3933.
5. Q. Shi, F. Liang, B. Cheadle, Corrosion 60, 5 (2004): p. 492-500.
6. A. Afseth, J.H. Nordlien, G.M. Scamans, K. Nisancioglu, Corrosion Science 43, 11 (2001): p. 2093-2109.
7. O. Seri, M. Imaizumi, Corrosion Science 30, 11 (1990): p. 1121-1133.
8. R.G. Buchheit, J Electrochem Soc 142, 11 (1995): p. 3994-3996.
9. K.M. Fleming, A. Zhu, J.R. Scully, Corrosion 68, 12 (2012): p. 1126-1145.
10. R.G. Buchheit, R.K. Boger, M.C. Carroll, R.M. Leard, C. Paglia, J.L. Searles, JOM 53, 7 (2001): p. 29-33.
11. M.K. Cavanaugh, J.-C. Li, N. Birbilis, R.G. Buchheit, J Electrochem Soc 161, 12 (2014): p. C535-C543.
12. N. Birbilis, R.G. Buchheit, J Electrochem Soc 155, 3 (2008): p. C117-C126.
13. M. Melander, R. Woods, Corrosion 66, 1 (2010): p. 015005-015005-015014.
14. S. Iwao, M. Yoshino, M. Edo, S. Kuroda, Corrosion 71, 5 (2014): p. 598-605.
15. A. Afseth, J.H. Nordlien, G.M. Scamans, K. Nisancioglu, Corrosion Science 43, 12 (2001): p. 2359-2377.
16. F. Andreatta, H. Terryn, J.H.W. de Wit, Electrochim. Acta 49, 17–18 (2004): p. 2851-2862.
17. S.Y. Chen, K.H. Chen, G.S. Peng, L. Jia, P.X. Dong, Materials & Design 35, (2012): p. 93-98.
18. K. El-Menshawy, A.W.A. El-Sayed, M.E. El-Bedawy, H.A. Ahmed, S.M. El-Raghy, Corrosion Science 54, (2012): p. 167-173.
19. W.D. Finnegan, R.A. Woods, 1995 Vehicle Thermal Management Systems, (1995): p. 275-288.
20. S. Iwao, M. Asano, Journal of Japan Institute of Light Metals 57, 2007 (2007): p. 589-594.
21. S. Iwao, M. Asano, Journal of Japan Institute of Light Metals 59, (2009):
22. T. Marlaud, B. Malki, A. Deschamps, B. Baroux, Corrosion Science 53, 4 (2011): p. 1394-1400.
23. J.M. Sanchez-Amaya, M. Bethencourt, L. Gonzalez-Rovira, F.J. Botana, Electrochim. Acta 52, 23 (2007): p. 6569-6583.
24. G. Svenningsen, M.H. Larsen, J.H. Nordlien, K. Nisancioglu, Corrosion Science 48, 12 (2006): p. 3969-3987.
25. G. Svenningsen, M.H. Larsen, J.H. Nordlien, K. Nisancioglu, Corrosion Science 48, 1 (2006): p. 258-272.
26. W.L. Zhang, G.S. Frankel, Electrochim. Acta 48, 9 (2003): p. 1193-1210.
27. S.K. Kairy, P.A. Rometsch, C.H.J. Davies, N. Birbilis, Corrosion 71, 11 (2015): p. 1304-1307.
28. S.K. Kairy, P.A. Rometsch, K. Diao, J.F. Nie, C.H.J. Davies, N. Birbilis, Electrochim. Acta 190, (2016): p. 92-103.
29. S.K. Kairy, T. Alam, P.A. Rometsch, C.H.J. Davies, R. Banerjee, N. Birbilis, Metallurgical and Materials Transactions A 47, 3 (2016): p. 985-989.
30. G. Svenningsen, J.E. Lein, A. Bjorgum, J.H. Nordlien, Y.D. Yu, K. Nisancioglu, Corrosion Science 48, 1 (2006): p. 226-242.
31. G. Svenningsen, M.H. Larsen, J.C. Walmsley, J.H. Nordlien, K. Nisancioglu, Corrosion Science 48, 6 (2006): p. 1528-1543.
32. F.N. Afshar, E. Szala, A. Wittebrood, A. Buerger, C.J.G. Van Hoek, J.M.C. Mol, H. Terryn, J.H.W. De Wit, Vehicle Thermal Management Systems Conference and Exhibition (Vtms 10), (2011): p. 69-79.
33. D.J. Schmatz, Weld J 62, 10 (1983): p. S267-S271.
34. A.J. Wittebrood, "Microstructural Changes in Brazing Sheet Due to Solid-Liquid Interaction" Diss Delft 2009, Corus Research, Development & Technology,
35. F.N. Afshar, R. Ambat, C. Kwakernaak, J.H.W. de Wit, J.M.C. Mol, H. Terryn, Electrochim. Acta 77, (2012): p. 285-293.
36. F.N. Afshar, J.H.W. de Wit, H. Terryn, J.M.C. Mol, Electrochim. Acta 88, (2013): p. 330-339.
37. F.N. Afshar, A.M. Glenn, J.H.W. de Wit, H. Terryn, J.M.C. Mol, Electrochim. Acta 104, (2013): p. 48-63.
38. J. Lacaze, S. Tierce, M.C. Lafont, Y. Thebault, N. Pebere, G. Mankowski, C. Blanc, H. Robidou, D. Vaumousse, D. Daloz, Mat Sci Eng a-Struct 413, (2005): p. 317-321.
39. J.-P.S.f.m. Properties, "Http://Www.Sentesoftware.Co.Uk," (Accessed : 7th February 2012),
40. I.R. Harrowfield, C.M. MacRae, N.C. Wilson, Microbeam Analysis Society, (1993): p. 547-548.
41. V. Guillaumin, P. Schmutz, G.S. Frankel, J Electrochem Soc 148, 5 (2001): p. B163-B173.
42. M. Rohwerder, E. Hornung, M. Stratmann, Electrochim. Acta 48, 9 (2003): p. 1235-1243.
43. S. Kuroda, K. Tohma, Journal of Japan Institute of Light Metals 48, 1 (1998):

FIGURE CAPTIONS

FIGURE 1. Summary of the important microstructural features on the cross-sectional optical images (a and c) and optical micrograph of the surface (b) of the as-brazed sheet structure after the brazing step.

FIGURE 2. JmatPro calculation for equilibrium phases in re-solidified clad in AA4xxx/AA3xxx as-brazed sheet. Chemical composition (table 1) and the temperature range (25-650 °C) are inputs for the JmatPro software calculations [39].

FIGURE 3. JmatPro calculation to predict the elemental composition changes of the α-Al(Fe, Mn) Si phase as a result of the heat treatment. Chemical composition (table 1) and the temperature range (100-650 °C) are the inputs for the JmatPro software calculations [39].

FIGURE 4. Volta potential difference (VPD) maps and position indication for section analysis profiles before and after the heat treatment processes.

FIGURE 5. line scan section analysis results, obtained from the SKPFM analyses of the polished surfaces after different heat treatment processes.

FIGURE 6. X-ray micro-analysis mappings of the Si and Cu alloying elements for the as-brazed and post-brazing heat treated substrates.

FIGURE 7. EPMA analysis maps of Cu in the as-brazed and post-brazing heat treated AA4xxx/AA3xxx aluminum material.

FIGURE 8. EPMA analysis maps of Si for the as-brazed and post-brazing heat treated AA4xxx/AA3xxx aluminum materials.

FIGURE 9. BF TEM micrographs collected from the core and clad regions of the as-brazed (a and c) and post-brazing heat treated (b and d) substrates.

FIGURE 10. TEM micrograph and EDX line-scan analysis of a grain boundary for the post-brazing heat treated clad material.

FIGURE 11. TEM bright field (a and b) micrographs of the core structure of a post-brazing heat treated sample. The HAADF (c) micrograph contains a diffraction contrast leading to different intensities of the two grains. The heavier precipitates are brighter. (d) shows the EDX line-scan analysis of the Cu K-line across the grain boundary of the post-brazing heat treated core material. Note that the Cu atomic % is a relative value as some Cu-containing parts of the specimen support grid contribute in the X-rays response.

FIGURE 12. Open-circuit corrosion potentials of the post-brazing heat treated clad material and core after 15 min of immersion in 42 gr/l NaCl solution at pH 2.8, before the anodic and cathodic polarizations.

FIGURE 13. Anodic (a) and cathodic (b) polarization curves before (as-brazed) and after the post-brazing heat treatment subjected to 15 min OCP measurements in 42 g/l NaCl solution at pH 2.8 (scan rate 0.5 mV/s).

FIGURE 14. Volta potential maps with line scan section analyses (a and b) and topographical maps (c and d), obtained from the AFM/SKPFM measurements of the polished surfaces before (as-brazed) and after the post-brazing heat treatment.

FIGURE 15. Box chart presentation of the Volta potential profiles collected from cross sections of the as-brazed and post-brazing heat treated substrates.

FIGURE 16. Topographical (a and b) and Volta potential maps (c and d) obtained from the AFM/SKPFM analyses of the as-brazed and post-brazing heat treated aluminum materials.

FIGURE 17. Optical micrographs of the cross sections collected from the as-brazed (a, b and c) and post-brazing heat treated (d, e and f) as-brazed aluminum sheet samples after anodic polarizations, 1 V above OCP values in a 42 g/l NaCl solution at pH 2.8.

FIGURE 18. Optical micrographs of the as-brazed (a and b) and post-brazing heat treated (c and d) aluminum samples after 30 days exposure to SWAAT solution (42 g/l NaCl solution at pH 2.8).

Table

Table 1. Chemical compositions (wt %) of the AA3xxx, i.e. core, and AA4xxx, i.e. clad, material.

	Si	Fe	Cu	Ti	V	Cr	Mn	Al
Clad	7.70	0.18	-	0.01	-	-	0.14	Bal.
Core	0.44	0.32	0.6	0.08	0.01	0.07	1.03	Bal.

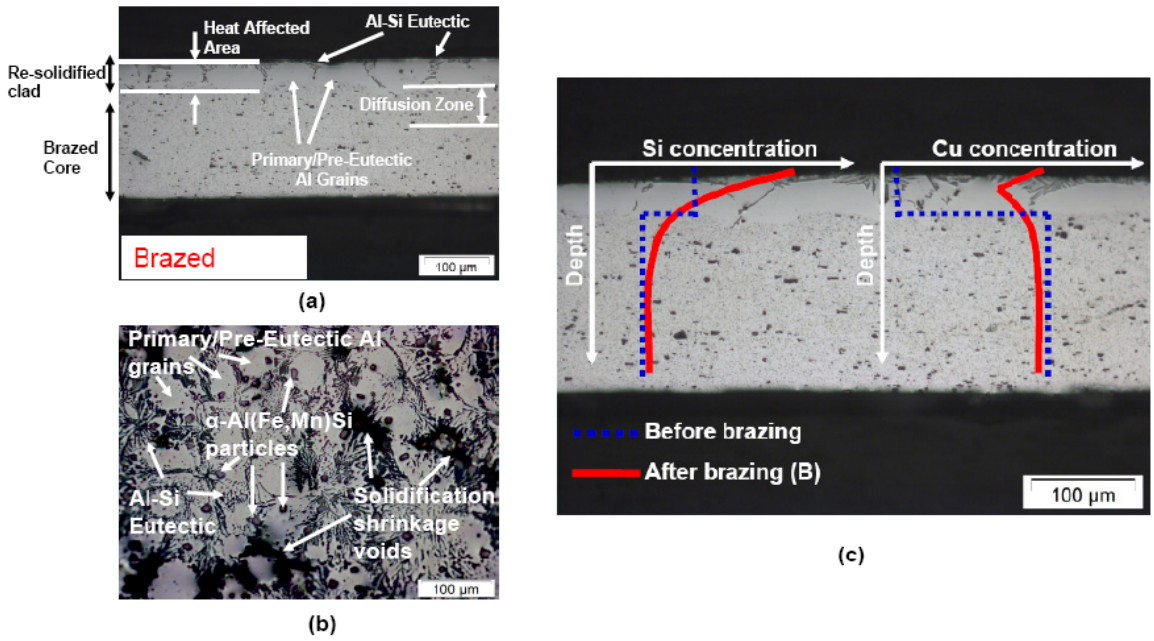

FIGURE 1. Summary of the important microstructural features on the cross-sectional optical images (a and c) and optical micrograph of the surface (b) of the as-brazed sheet structure after the brazing step.

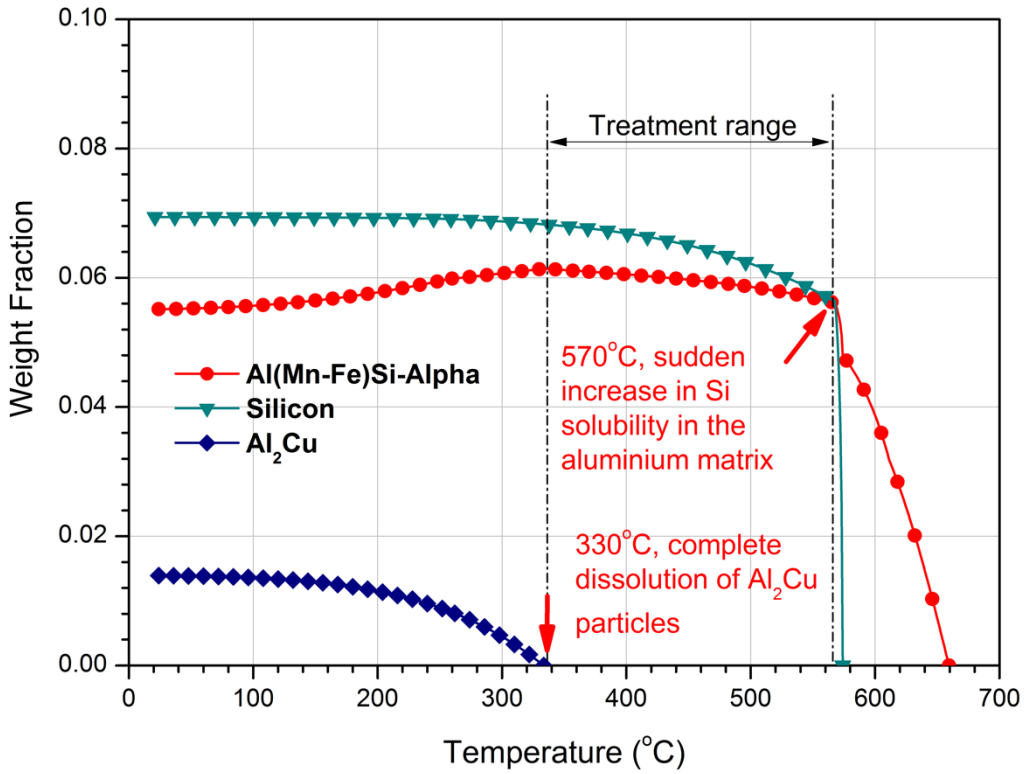

FIGURE 2. JmatPro calculation for equilibrium phases in re-solidified clad in AA4xxx/AA3xxx as-brazed sheet. Chemical composition (table 1) and the temperature range (25-650 °C) are inputs for the JmatPro software calculations [39].

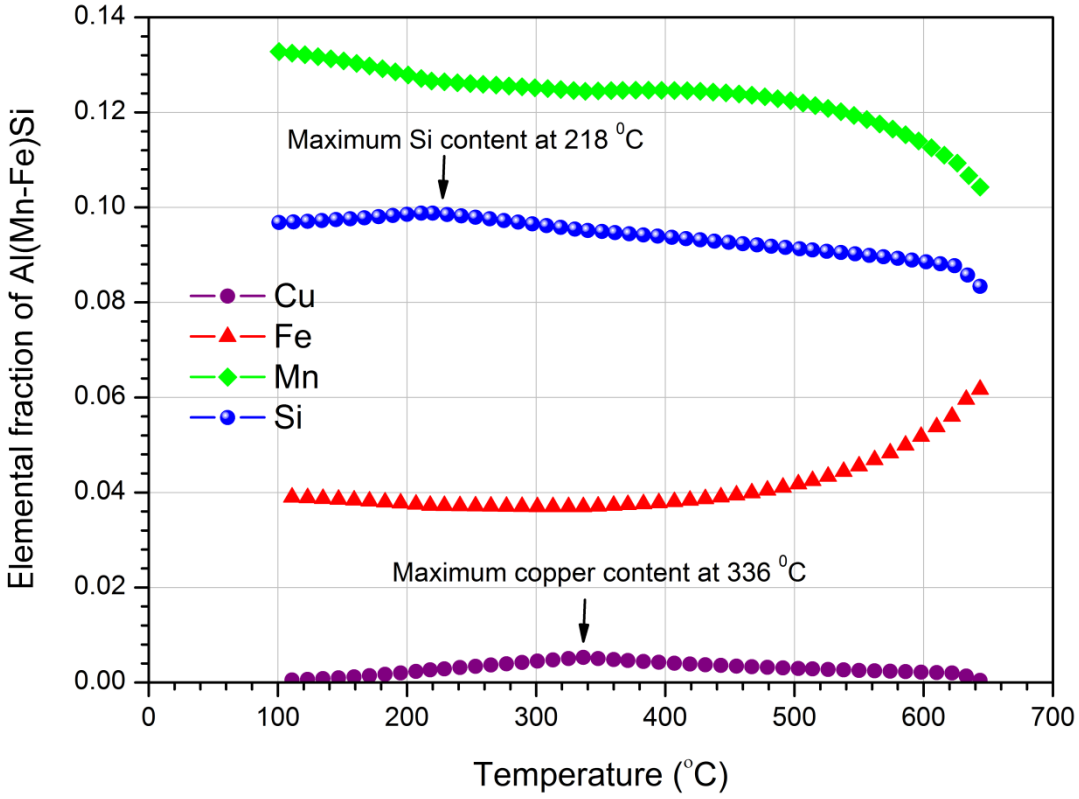

FIGURE 3. JmatPro calculation to predict the elemental composition changes of the α-Al(Fe, Mn) Si phase as a result of the heat treatment. Chemical composition (table 1) and the temperature range (100-650 °C) are the inputs for the JmatPro software calculations [39].

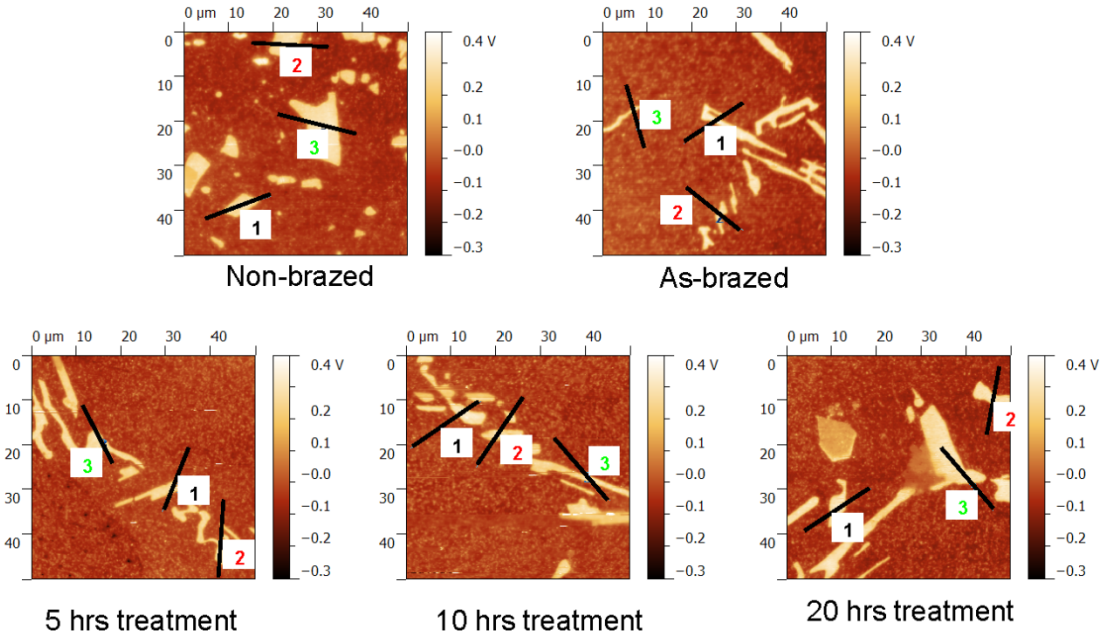

FIGURE 4. Volta potential difference (VPD) maps and position indication for section analysis profiles before and after the heat treatment processes.

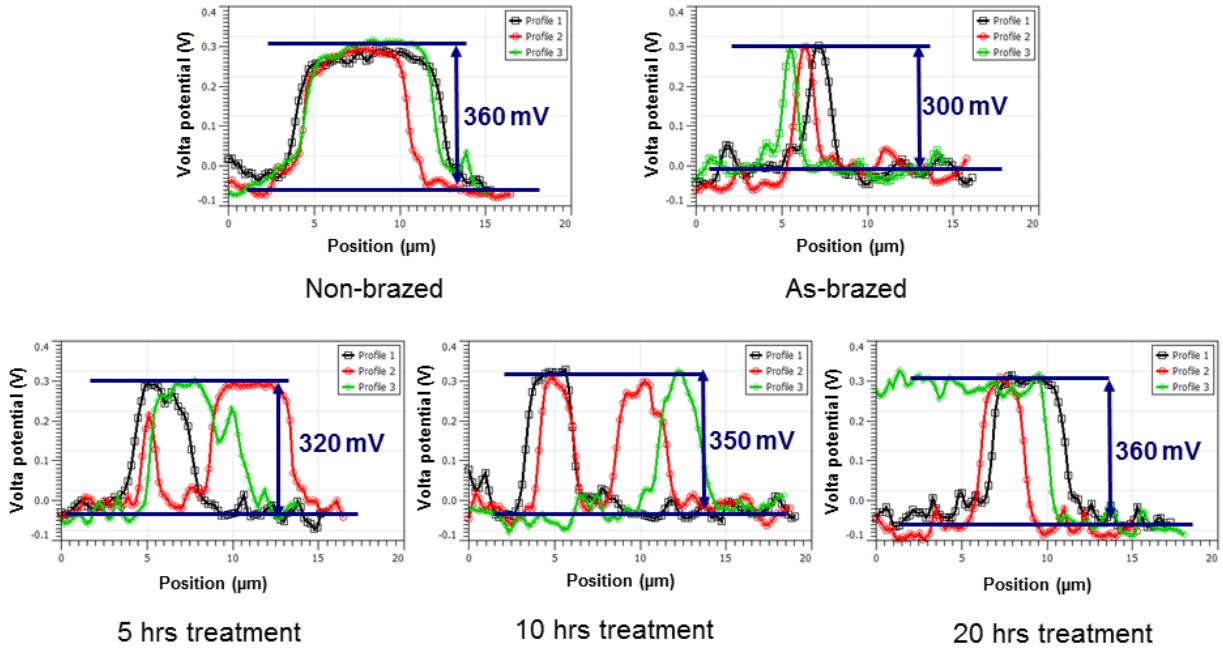

FIGURE 5. line scan section analysis results, obtained from the SKPFM analyses of the polished surfaces after different heat treatment processes.

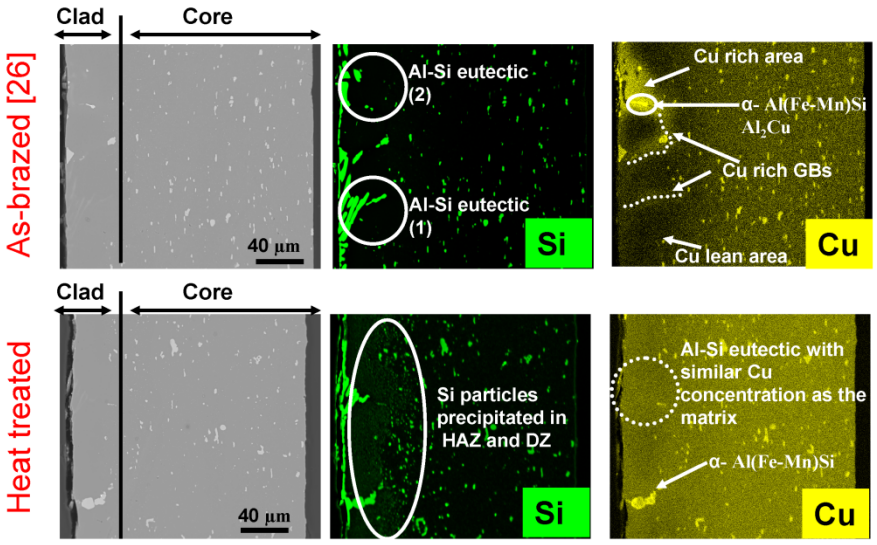

FIGURE 6. X-ray micro-analysis mappings of the Si and Cu alloying elements for the as-brazed and post-brazing heat treated substrates.

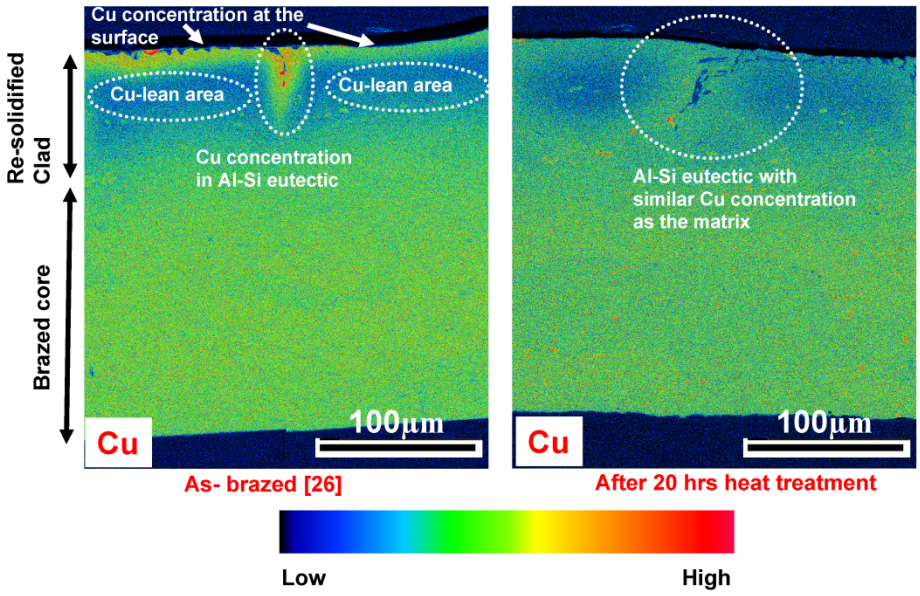

FIGURE 7. EPMA analysis maps of Cu in the as-brazed and post-brazing heat treated AA4xxx/AA3xxx aluminum material.

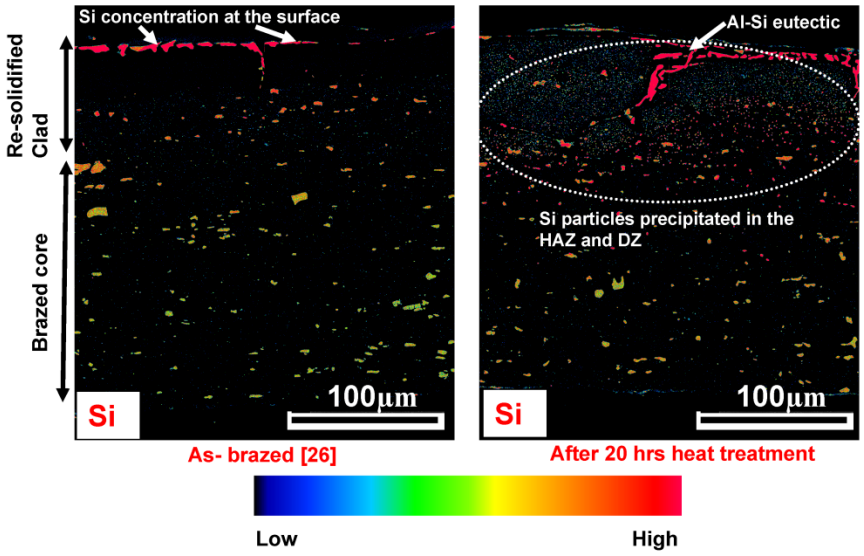

FIGURE 8. EPMA analysis maps of Si for the as-brazed and post-brazing heat treated AA4xxx/AA3xxx aluminum materials.

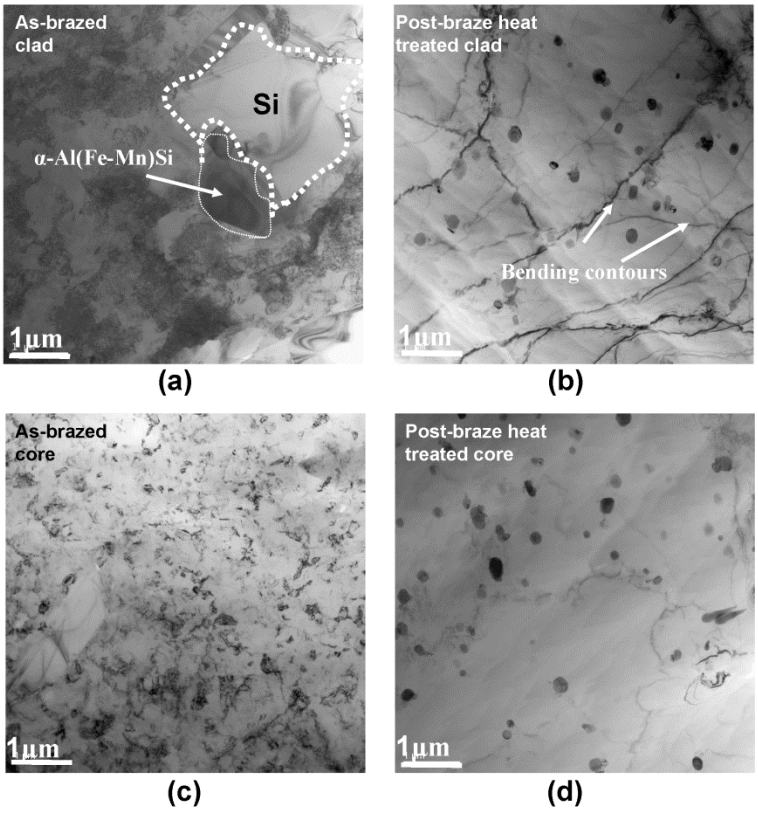

FIGURE 9. BF TEM micrographs collected from the core and clad regions of the as-brazed (a and c) and post-brazing heat treated (b and d) substrates.

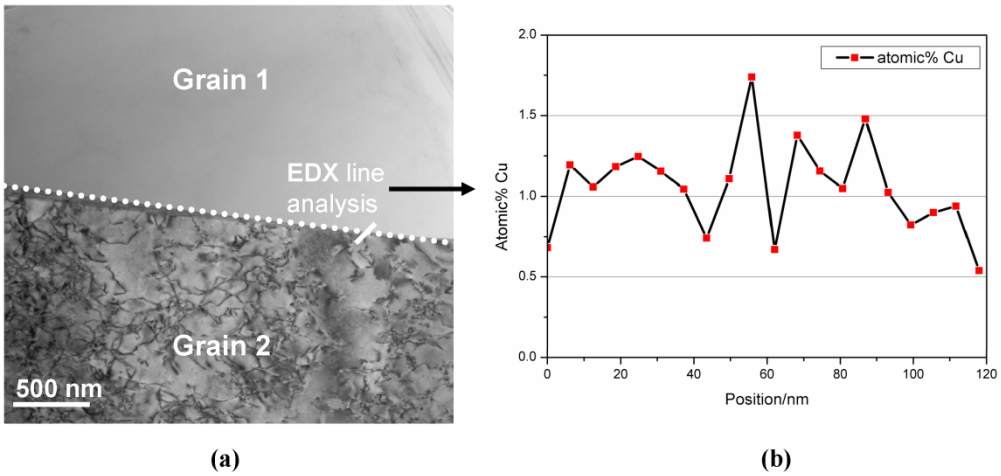

FIGURE 10. TEM micrograph and EDX line-scan analysis of a grain boundary for the post-brazing heat treated clad material.

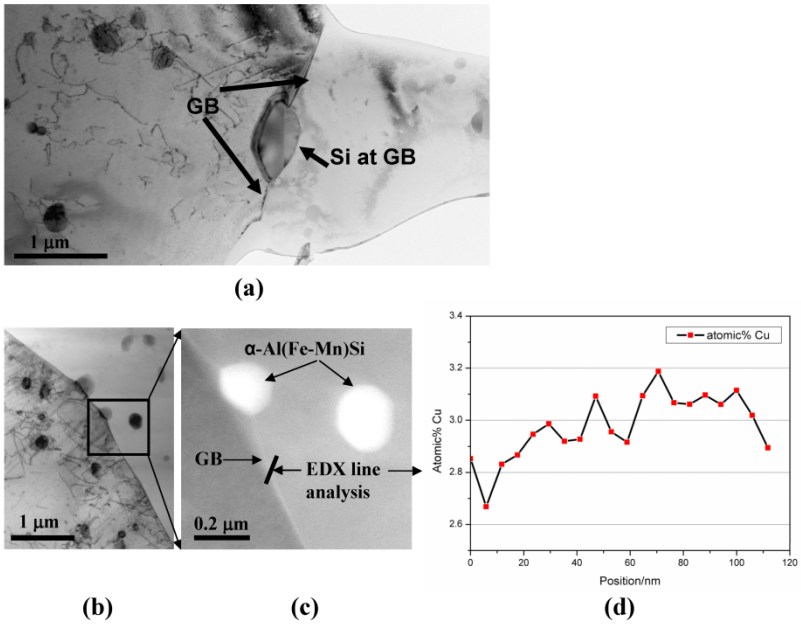

FIGURE 11. TEM bright field (a and b) micrographs of the core structure of a post-brazing heat treated sample. The HAADF (c) micrograph contains a diffraction contrast leading to different intensities of the two grains. The heavier precipitates are brighter. (d) shows the EDX line-scan analysis of the Cu K-line across the grain boundary of the post-brazing heat treated core material. Note that the Cu atomic % is a relative value as some Cu-containing parts of the specimen support grid contribute in the X-rays response.

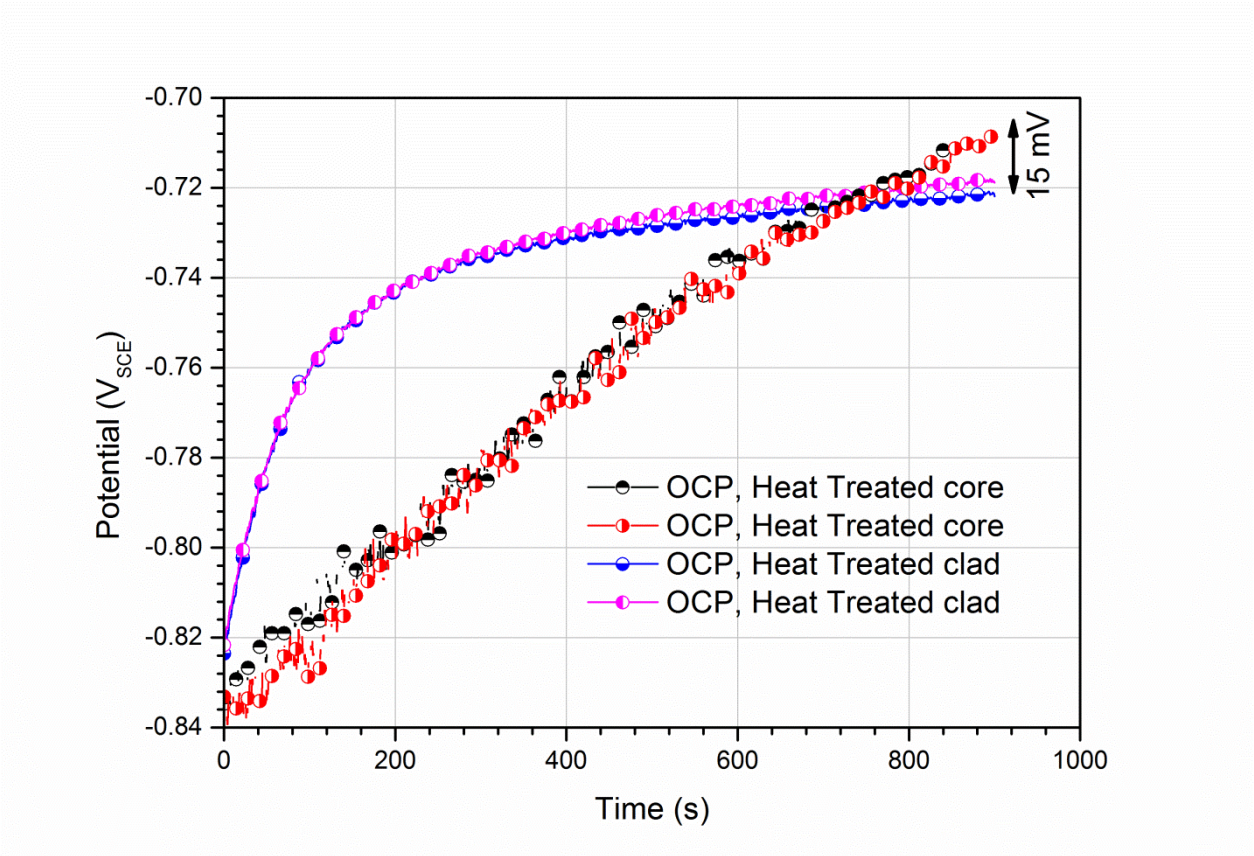

FIGURE 12. Open-circuit corrosion potentials of the post-brazing heat treated clad material and core after 15 min of immersion in 42 gr/l NaCl solution at pH 2.8, before the anodic and cathodic polarizations.

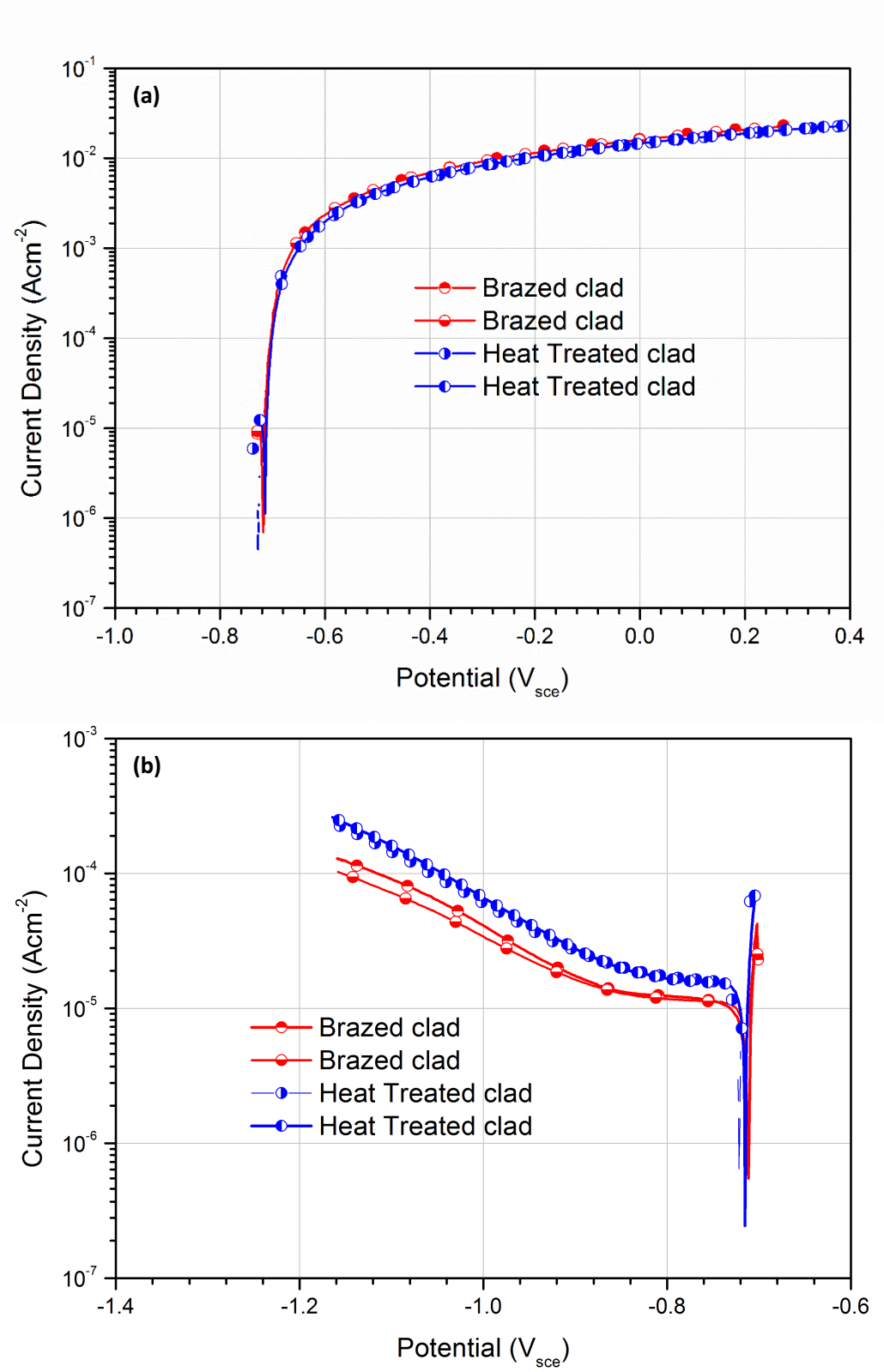

FIGURE 13. Anodic (a) and cathodic (b) polarization curves before (as-brazed) and after the post-brazing heat treatment subjected to 15 min OCP measurements in 42 g/l NaCl solution at pH 2.8 (scan rate 0.5 mV/s).

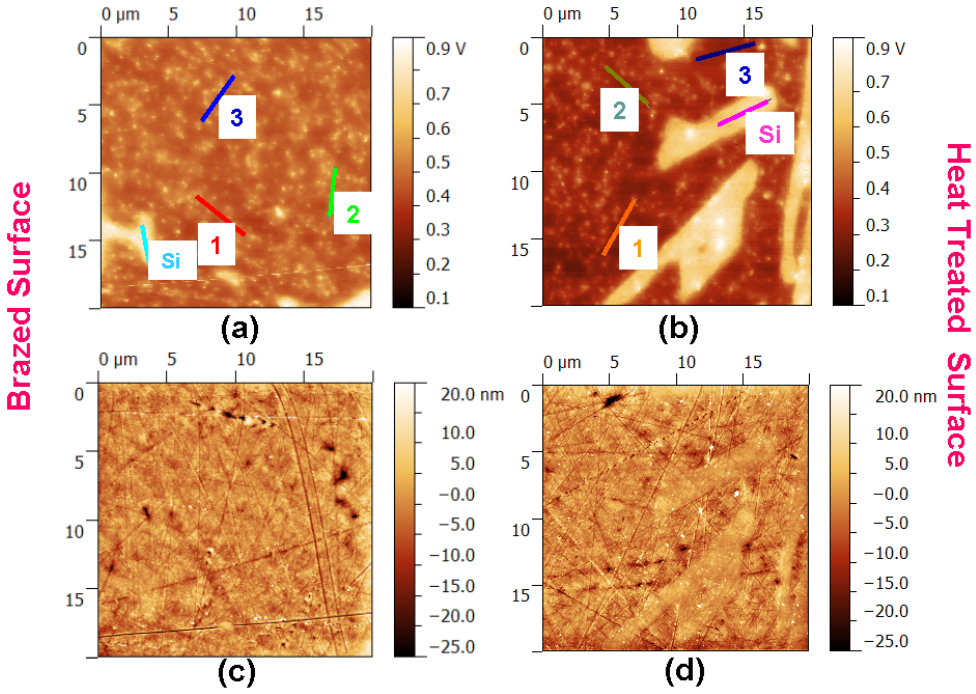

FIGURE 14. Volta potential maps with line scan section analyses (a and b) and topographical maps (c and d), obtained from the AFM/SKPFM measurements of the polished surfaces before (as-brazed) and after the post-brazing heat treatment.

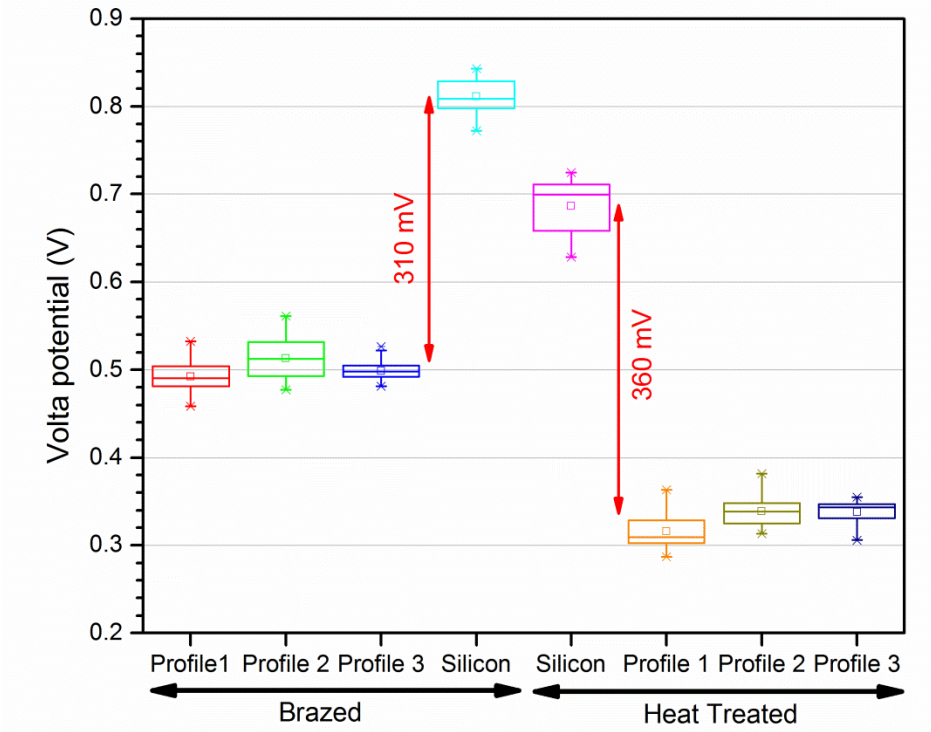

FIGURE 15. Box chart presentation of the Volta potential profiles collected from cross sections of the as-brazed and post-brazing heat treated substrates.

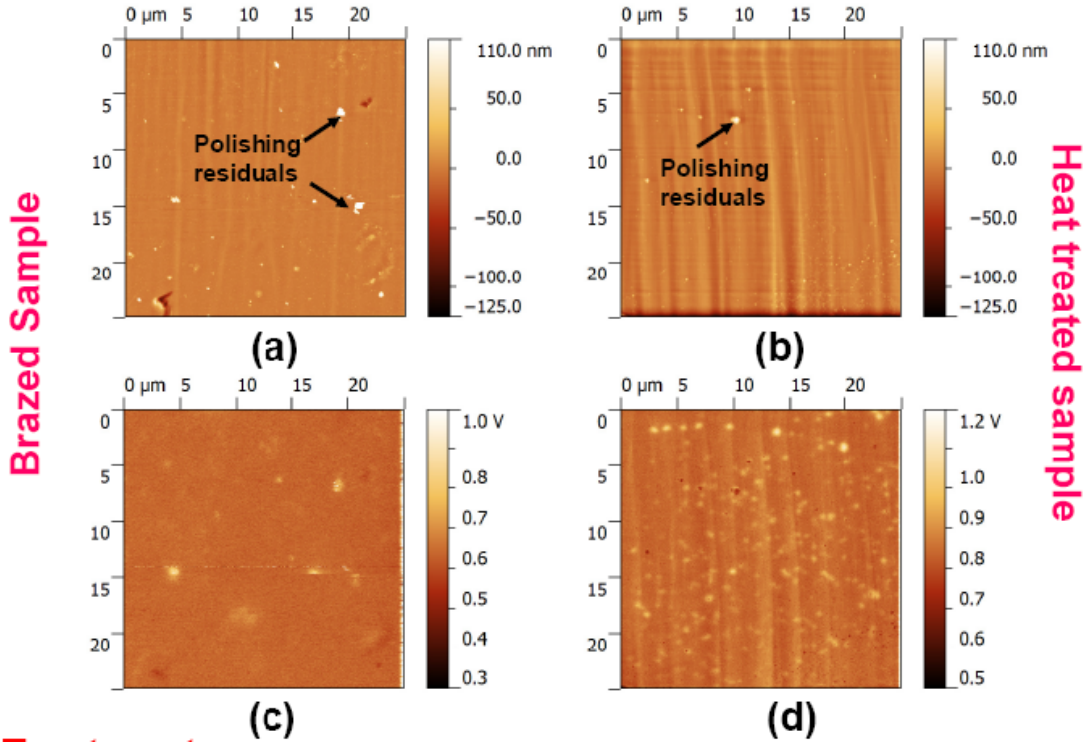

FIGURE 16. Topographical (a and b) and Volta potential maps (c and d) obtained from the AFM/SKPFM analyses of the as-brazed and post-brazing heat treated aluminum materials.

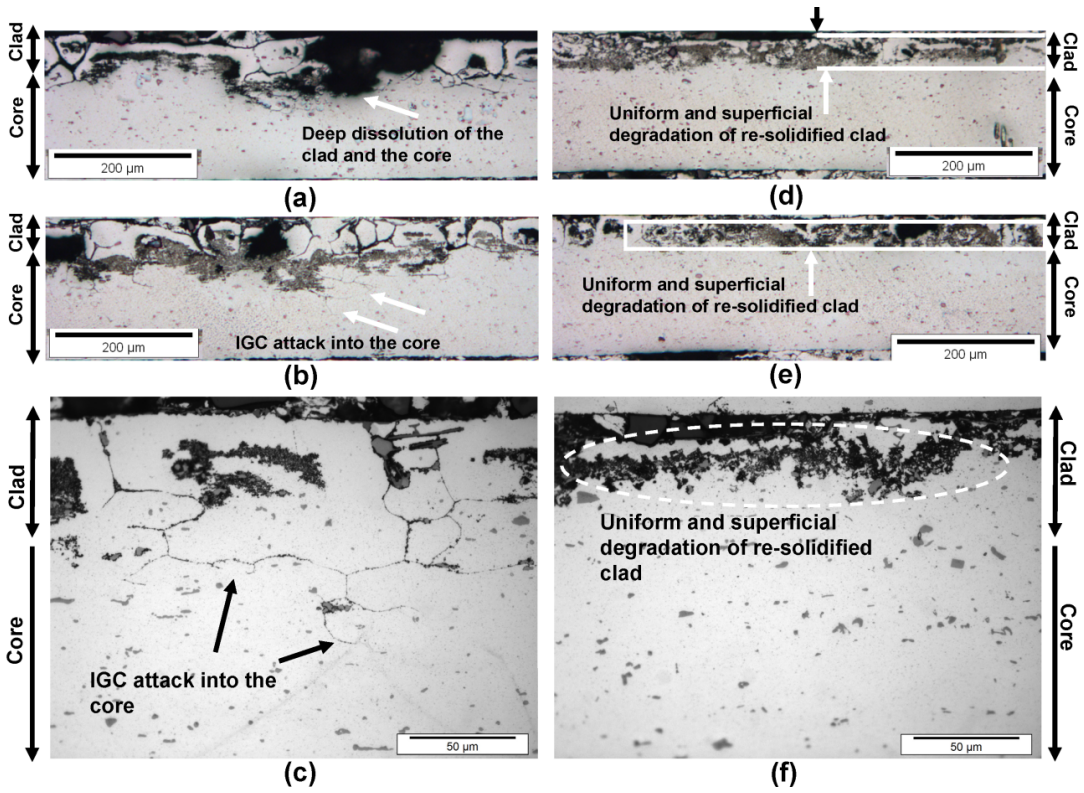

FIGURE 17. Optical micrographs of the cross sections collected from the as-brazed (a, b and c) and post-brazing heat treated (d, e and f) as-brazed aluminum sheet samples after anodic polarizations, 1 V above OCP values in a 42 g/l NaCl solution at pH 2.8.

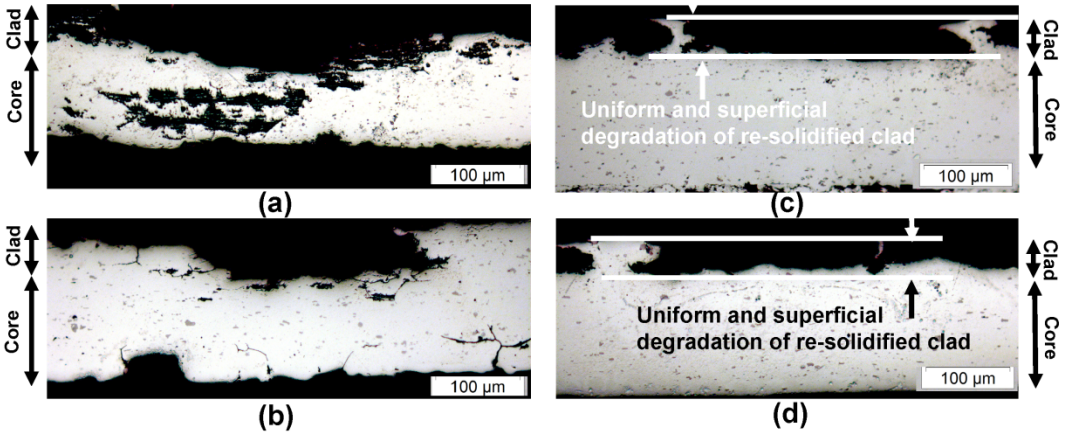

FIGURE 18. Optical micrographs of the as-brazed (a and b) and post-brazing heat treated (c and d) aluminum samples after 30 days exposure to SWAAT solution (42 g/l NaCl solution at pH 2.8)